

Characterization of tandem aerosol classifiers for selecting particles: implication for eliminating multiple charging effect

Yao Song¹, Xiangyu Pei¹, Huichao Liu¹, Jijia Zhou¹, Zhibin Wang^{1,2,3*}

¹ College of Environmental and Resource Sciences, Zhejiang Provincial Key Laboratory of Organic Pollution Process and Control, Zhejiang University, Hangzhou 310058, China

²ZJU-Hangzhou Global Scientific and Technological Innovation Center, Hangzhou 311200, China

³Key Laboratory of Environment Remediation and Ecological Health, Ministry of Education, Zhejiang University, Hangzhou 310058, China

Correspondence to: Zhibin Wang (wangzhibin@zju.edu.cn)

Abstract. Accurate particle classification plays a vital role in aerosol studies. Differential mobility analyzer (DMA), centrifugal particle mass analyzer (CPMA) and aerodynamic aerosol classifier (AAC) are commonly used to select particles with a specific mobility diameter, aerodynamic diameter or mass, respectively. However, multiple charging effects cannot be entirely avoided when using either individual techniques or tandem systems such as DMA-CPMA, especially when selecting soot particles with fractal structures. In this study, we calculate the transfer functions of the DMA-CPMA and DMA-AAC in static configurations for flame generated soot particles. We propose an equation that constrains the resolutions of DMA and CPMA to eliminate the multiple charging effect when selecting particles with a certain mass-mobility relationship using the DMA-CPMA system. The equation for the DMA-AAC system is also derived. For DMA-CPMA in a static configuration, our results show that the ability to remove multiply charged particles mainly depends on the particle morphology and resolution settings of the DMA and CPMA. Using measurements from soot experiments and literature data, a general trend in the appearance of multiple charging effect with decreasing size when selecting aspherical particles is observed. As for DMA-AAC in a static configuration, the ability to eliminate particles with multiple charges is mainly related to the resolutions of the classifiers. In most cases, the DMA-AAC in a static configuration can eliminate multiple charging effect regardless of the particle morphology, but multiply charged particles will be selected when decreasing the resolution of the DMA or AAC. We propose that the potential influence of the multiple charging effect should be considered when using the DMA-CPMA or DMA-AAC systems in estimating size- and mass-resolved optical properties in field and lab experiments.

1 Introduction

Atmospheric aerosol particles span a wide size range from 1 nm to > 100 μm . A significant size dependence of aerosol physicochemical properties has been widely reported. Particle size can strongly alter the hygroscopic behavior (Biskos et al., 2006), phase state (Cheng et al., 2015) and cloud-nucleating ability

35 (Dusek et al., 2006) of aerosol nanoparticles, indicating the importance of particle size when assessing the
36 climate effect. Hence, accurate particle classification is essential when investigating the size dependent
37 behavior of aerosol particles.

38 At present, particles are generally classified by either size or mass in atmospheric aerosol studies. A
39 differential mobility analyzer (DMA) is the most commonly used size classifier, which selects particles based
40 on electrical mobility (Knutson and Whitby, 1975; Park et al., 2008; Stolzenburg and McMurry, 2008;
41 Swietlicki et al., 2008; Wiedensohler et al., 2012). A particle mass analyzer (PMA) includes an aerosol
42 particle mass analyzer (APM) and a centrifugal particle mass analyzer (CPMA), both of which classify
43 particles based on their mass-to-charge ratio (Ehara et al., 1996; Olfert and Collings, 2005). The charge
44 distribution of particles must be known by passing through a neutralizer or similar when classified by DMA
45 or PMA. However, particles with higher-order charges and identical apparent mobility or mass-to-charge
46 ratio can be selected simultaneously, which are referred to as the multiple charging effect. This may introduce
47 uncertainty in the subsequent characterization. Radney et al. (2013) demonstrated that although single-
48 charged particles account for the highest number fraction (46.3%) of DMA-classified particles (200 nm),
49 their contributions to the total mass concentration and extinction are insignificant (10.8% and 7.96%,
50 respectively). Thus, the reported extinction of particles with a certain diameter has been greatly overestimated
51 due to the multiple charging effect.

52 Previous studies (Shiraiwa et al., 2010; Rissler et al., 2013; Johnson et al., 2014; Johnson et al., 2021) tried to
53 utilize the combination of size and mass classifiers, such as DMA-APM or DMA-CPMA systems, to obtain
54 singly charged particles. Theoretically, the ability of a DMA-APM to eliminate multiply charged particles is
55 governed by the particle morphology and setups of the DMA and APM (Kuwata, 2015). This conclusion
56 implies that multiply charged particles cannot be effectively excluded for aspherical particles, especially for
57 soot particles. Radney and Zangmeister (2016) investigated the limitations of a DMA-APM with three types
58 of particles (polystyrene latex (PSL) spheres, ammonium sulfate (AS) and soot particles). Their results
59 demonstrated that a DMA-APM can resolve multiply charged particles for spherical particles (PSL and AS
60 particles), but it failed for aspherical soot particles. Multiply charged soot particles led to over 110% errors
61 in retrieving the mass specific extinction cross section.

62 In contrast to DMA and PMA, an aerodynamic aerosol classifier (AAC) is a novel instrument that selects the
63 aerodynamic equivalent diameter of aerosol particles based on their relaxation time. The advantage of
64 utilizing an AAC is that the charge state of the particles does not need to be known in particle classification
65 compared with the aforementioned classifiers; hence, multiple charging effects can be avoided (Tavakoli and
66 Olfert, 2013). However, the selected particles are not monodispersed in mobility diameter when an AAC is
67 used to select aspherical particles (Kazemimanesh et al., 2022).

68 Morphology information, such as effective density (ρ_{eff}), mass–mobility exponent (D_{fm}) and dynamic shape
69 factor (χ), can be inferred using tandem DMA-PMA system (Park et al., 2003; Zhang et al., 2008; Rissler et
70 al., 2013; Pei et al., 2018; Zangmeister et al., 2018), DMA-AAC (Tavakoli and Olfert, 2014) and AAC-
71 CPMA systems (Kazemimanesh et al., 2022). The derived ρ_{eff} and χ depend upon the combination of

72 instruments used, while the nonphysical values of χ and ρ_{eff} for aspherical particles can be determined by the
73 AAC-APM (Yao et al., 2020) and AAC-CPMA (Kazemimanesh et al., 2022).
74 The theoretical transfer functions of individual classifiers (DMA, CPMA and AAC) and the DMA-APM
75 system have been previously discussed (Knutson and Whitby, 1975; Ehara et al., 1996; Olfert and Collings,
76 2005; Stolzenburg and McMurry, 2008; Tavakoli and Olfert, 2013). In this study, we focus on a DMA-
77 CPMA and DMA-AAC in static configurations to eliminate multiply charged particles. The DMA-CPMA
78 and DMA-AAC systems mentioned below refer to the tandems of a DMA and CPMA or a DMA and AAC
79 in a static configuration, respectively. We calculate the transfer functions of the DMA-AAC and DMA-
80 CPMA systematically. Combined with soot experiments, we demonstrate that multiple charging effects may
81 still exist after DMA-CPMA classification when selecting aspherical particles and evaluate the light
82 absorption of selected particles with different charging states using Mie theory. Furthermore, we propose
83 operating conditions for the DMA-CPMA and DMA-AAC to eliminate multiply charged particles in future
84 studies. Our results suggest that the size- and mass-resolved optical properties may be overestimated for
85 small soot particles when using the DMA-CPMA system, which will lower the prediction accuracy of the
86 fresh soot climate effect. In Sect. 3.1, we calculate the transfer functions of the DMA-CPMA and DMA-
87 AAC utilizing the literature data of soot particles from Pei et al. (2018). In Sect. 3.2, we measure the multiple
88 charging effect of the DMA-CPMA using laboratory-generated soot particles, and the bias of optical
89 measurement induced by multiply charged particles is evaluated in Sect. 3.3.

90 **2 Theory and experiment**

91 **2.1 Transfer function for individual aerosol classifiers**

92 **DMA**

93 The DMA, consisting of two coaxial electrodes, classifies particles based upon electrical mobility Z_p
94 (Knutson and Whitby, 1975), which can be calculated as follows:

$$95 \quad Z_p = qB = \frac{neCc(d_m)}{3\pi\mu d_m}, \quad (1)$$

96 where q is the particle charge, n is the number of elementary charges, B is the mobility of the particle, e is
97 the elementary charge, μ is the viscosity of air, and $Cc(d_p)$ is the Cunningham slip correction factor. When
98 the aerosol inlet flow rate equals the aerosol sampling outlet flow rate, the centroid mobility, Z_p^* , selected by
99 the DMA is defined as

$$100 \quad Z_p^* = \frac{Q_{\text{sh}}}{2\pi V_{\text{DMA}} L_{\text{DMA}}} \ln\left(\frac{r_{2_DMA}}{r_{1_DMA}}\right), \quad (2)$$

101 where Q_{sh} is the sheath flow rate, V_{DMA} is the voltage between the two electrodes, L_{DMA} is the length of the
102 DMA, and r_{1_DMA} and r_{2_DMA} are the inner and outer radii of the DMA electrodes, respectively. Assuming
103 that the aerosol inlet and aerosol sampling flow rates are equal, the transfer function of the DMA can be
104 expressed as follows when particle diffusion is negligible (Knutson and Whitby, 1975; Stolzenburg and
105 McMurry, 2008):

$$\Omega(\tilde{Z}_p, \beta_{\text{DMA}}) = \frac{1}{2\beta_{\text{DMA}}} [|\tilde{Z}_p - (1 + \beta_{\text{DMA}})| + |\tilde{Z}_p - (1 - \beta_{\text{DMA}})| - 2|\tilde{Z}_p - 1|], \quad (3)$$

where, $\tilde{Z}_p = Z_p/Z_p^*$, $\beta_{\text{DMA}} = Q_a/Q_{\text{sh}}$, and Q_a is the sample flow rate. The limiting electrical mobilities that DMA can select are $(1 \pm \beta_{\text{DMA}}) \cdot Z_p^*$. The maximum and minimum values of d_m for particles with n charges can be derived combining $(1 \pm \beta_{\text{DMA}}) \cdot Z_p^*$ and Eq. (1), and denote as $d_{m,\text{max}}$ and $d_{m,\text{min}}$, respectively. The transfer function is an isosceles triangle with value of 1 at Z_p^* and going to 0 at $(1 \pm \beta_{\text{DMA}}) \cdot Z_p^*$. It translates to asymmetry in d_m since the relationship between d_m and Z_p is nonlinear.

112 CPMA

113 The APM consists of two coaxial electrodes which are rotating at an equal angular velocity and a voltage is
 114 applied between these electrodes to create an electrostatic field (Ehara et al., 1996). The construction of the
 115 CPMA is similar to the APM, but its inner cylinder rotates faster than the outer cylinder to create a stable
 116 system of forces (Olfert and Collings, 2005). In the CPMA, the equation of particle motion is expressed as

$$117 \frac{m}{\tau} \frac{dr}{dt} = \frac{mv_\theta(r)^2}{r} - \frac{qV_{\text{CPMA}}}{r \ln\left(\frac{r_{2_CPMA}}{r_{1_CPMA}}\right)}, \quad (4)$$

118 and the trajectory equation is

$$119 \frac{dr}{dz} = \frac{dr}{dt} \left(\frac{dz}{dt}\right)^{-1} = \frac{c_r}{v_z}, \quad (5)$$

120 where τ is the relaxation time, m is the mass of the particle, t is time, V is the voltage difference between the
 121 two electrodes, and r_{1_CPMA} and r_{2_CPMA} are the radii of the inner and outer electrodes, respectively. c_r is the
 122 particle migration velocity, v_z is the axial flow distribution and v_θ is the velocity profile in the angular
 123 direction,

$$124 v_\theta = \omega_1 \frac{\hat{r}^2 - \hat{\omega}}{\hat{r}^2 - 1} r + \omega_1 r_{1_CPMA}^2 \frac{\hat{\omega} - 1}{\hat{r}^2 - 1} \frac{1}{r} = \alpha r + \frac{\beta}{r}, \quad (6)$$

125 where $\hat{\omega} = \omega_2/\omega_1$ is the ratio of the rotational speed of the outer electrode to the inner electrode and ω_1 and
 126 ω_2 are the rotational speeds of the inner and outer electrodes, respectively. \hat{r} is the ratio of the inner and outer
 127 radii. α and β are the azimuthal flow velocity distribution parameters.

128 Sipkens et al. (2019) presented methods to calculate the transfer function of the CPMA. They considered the
 129 Taylor series expansion about the center of the gap ($r_c = (r_{2_CPMA} + r_{1_CPMA})/2$) instead of the equilibrium radius
 130 to avoid problems with the scenario in which the equilibrium radius does not exist. This method is much
 131 simpler and more robust. In this case, the particle migration velocity in the radial direction is

$$132 c_r \approx C_3 + C_4(r - r_c), \quad (7)$$

133 where

$$134 C_3 = \tau \left(\alpha^2 r_c + \frac{2\alpha\beta}{r_c} + \frac{\beta^2}{r_c^3} - \frac{C_0}{mr_c} \right), \quad (8)$$

$$135 C_4 = \tau \left(\alpha^2 - \frac{2\alpha\beta}{r_c} - \frac{3\beta^2}{r_c^3} + \frac{C_0}{mr_c^2} \right), \quad (9)$$

$$136 C_0 = \frac{qV_{\text{CPMA}}}{\ln(r_{2_CPMA}/r_{1_CPMA})}, \quad (10)$$

137 Assuming plug flow, the transfer function would be

$$138 \Omega = \frac{r_b - r_a}{2\delta}, \quad (11)$$

139 where $\delta=(r_{2_CPMA}-r_{1_CPMA})/2$ is the half width of the gap between the two electrodes, and

$$140 \quad r_a = \min \left\{ r_{2_CPMA}, \max \{ r_{1_CPMA}, G_0(r_{1_CPMA}) \} \right\}, \quad (12)$$

$$141 \quad r_b = \min \left\{ r_{2_CPMA}, \max \{ r_{1_CPMA}, G_0(r_{2_CPMA}) \} \right\}, \quad (13)$$

$$142 \quad G_0(r_L) = r_c + \left(r_L - r_c + \frac{C_3}{C_4} \right) \exp(-C_4 L \bar{v}) - \frac{C_3}{C_4}, \quad (14)$$

143 where $G_0(r)$ is the operator used to map the final radial position of the particle to its position at the inlet and
 144 \bar{v} is the average flow velocity. $\min\{\}$ and $\max\{\}$ are the minimum and maximum values of the quantities in
 145 the brackets, respectively.

146 Reavell et al. (2011) calculated the resolution of the CPMA assuming that the gap between two electrodes is
 147 narrow enough that the variation of force in the gap can be ignored. The mass resolution (R_m) of CPMA is
 148 related to particles mobility. When selecting the particles with mass of m_1 and mobility of B_1 , the R_m can be
 149 calculated by

$$150 \quad R_m = \frac{2\pi B_1 L_{CPMA} r_c^2 \omega^2 m_1}{Q_{CPMA}}, \quad (15)$$

151 where ω is the equivalent rotational speed calculated by $\omega = \alpha + \frac{\beta}{r_c^2}$, m_1 is the nominal mass that the CPMA

152 can select, Q_{CPMA} is the volumetric flow rate. The limiting mass can be calculated by

$$153 \quad m_{n,\min}^{n,\max} = n \cdot m_1 \pm \frac{Q_{CPMA}}{2\pi B_{n,\min}^{n,\max} L_{CPMA} r_c^2 \omega^2} = n \cdot m_1 \pm \frac{m_1}{R_m} \cdot \frac{B_1}{B_{n,\min}^{n,\max}}, \quad (16)$$

154 where $m_{n,\min}^{n,\max}$ and $B_{n,\min}^{n,\max}$ are the maximum and minimum mass and corresponding mobility of particles
 155 bearing number of elementary charges of n that the CPMA can select, respectively. Further details can be
 156 found in Reavell et al. (2011) and Sipkens et al. (2019).

157 AAC

158 The AAC classifies particles based on relaxation time, which is defined by

$$159 \quad \tau = Bm = \frac{Cc(d_{ae})\rho_0 d_{ae}^2}{18\mu}, \quad (17)$$

160 where μ is the viscosity of air. $Cc(d_{ae})$ is the slip correction factor. ρ_0 is the standard density with a value of 1
 161 g/cm³ (Johnson et al. 2018). When the aerosol inlet flow rate equals the aerosol sampling outlet flow rate, it
 162 can be expressed as (Tavakoli and Olfert, 2013)

$$163 \quad \Omega = \frac{1}{2\beta_{AAC}} [|\tilde{\tau} - (1 - \beta_{AAC})| + |\tilde{\tau} - (1 + \beta_{AAC})| - 2|\tilde{\tau} - 1|], \quad (18)$$

164 τ^* is the nominal relaxation time, which is classified by the AAC,

$$165 \quad \tau^* = \frac{2Q_{sh}}{\pi\omega^2(r_{1_AAC}+r_{2_AAC})^2L}, \quad (19)$$

166 where $\beta_{AAC} = \frac{Q_a}{Q_{sh}}$, $\tilde{\tau} = \frac{\tau}{\tau^*}$, r_{1_AAC} and r_{2_AAC} are the inner and outer radii of the AAC, respectively. The
 167 limiting τ that AAC can select are $(1 \pm \beta_{AAC}) \cdot \tau^*$. The maximum and minimum values of d_{ae} can be derived
 168 and denoted as $d_{ae,\max}$ and $d_{ae,\min}$, respectively.

169 **2.2 Experimental setup**

170 A schematic of the experimental setup is illustrated in Fig. 1. Soot particles were generated by a miniature
 171 inverted soot generator (Argonaut Scientific Ltd., Canada) with a propane flow of 74.8 SCPM (standard mL
 172 per minute, flow in mL min⁻¹ converted from ambient to T =298.15 K and P = 101.325 kPa) and an air flow
 173 rate of 12 SLPM (Standard L per minute, flow in L min⁻¹ converted from ambient to T =298.15 K and P =
 174 101.325 kPa). Although this operation setting is not in the open-tip flame regime, the flame is open-tip
 175 consistent with Fig. 2d in Moallemi et al. (2019). Detailed aerosol generation methods can be found in
 176 Kazemimanesh et al. (2019b) and Moallemi et al. (2019). The polydispersed aerosols were dried to a relative
 177 humidity of <20% by a silica dryer and then passed through a soft X-ray neutralizer (Model 3088, TSI, Inc.,
 178 USA). Five mobility diameters (80 nm, 100 nm, 150 nm, 200 nm and 250 nm) of soot particles were selected
 179 with the DMA (Model 3081, TSI Inc., USA, $\beta_{DMA} = 10$). For the soot characterization, the mobility-selected
 180 aerosol flow was switched between two parallel lines and fed into the CPMA (Cambustion Ltd., UK) and
 181 AAC (Cambustion, Ltd., UK, $\beta_{AAC} = 10$); meanwhile, the condensation particle counter (CPC, Model 3756,
 182 TSI, Inc., USA, 0.3 L min⁻¹) was switched between the CPMA and AAC. The distributions of particle number
 183 concentration as a function of particle mass (m) and aerodynamic diameter (d_{ae}) were measured by the
 184 scanning mode of the CPMA and AAC, respectively, while the CPC recorded their corresponding number
 185 concentrations at each setpoint. For each d_m , the m and d_{ae} distributions were measured three times. Between
 186 measurements of each d_m , the CPC was used behind the DMA, and the number size distribution of the
 187 generated soot particles was measured by a scanning mobility particle sizer (SMPS) to ensure the number
 188 size distribution of generated soot particles did not change during the whole experiment. The m and d_{ae}
 189 distributions were fitted to log-normal distributions; thus, the modal values denoted as m_c and $d_{ae,c}$ for the
 190 mobility-selected particles were determined. The equation of log-normal distribution used in this study is
 191 expressed as

$$192 \begin{cases} N(m) = \frac{N_0}{\sqrt{2\pi\ln\sigma_m}} \exp\left(\frac{-(\log(m)-\log(m_c))^2}{2(\ln\sigma_m)^2}\right) \\ N(d_{ae}) = \frac{N_0}{\sqrt{2\pi\ln\sigma_{ae}}} \exp\left(\frac{-(\log(d_{ae})-\log(d_{ae,c}))^2}{2(\ln\sigma_{ae})^2}\right) \end{cases}, \quad (20)$$

193 where σ_m and σ_{ae} are the geometric standard deviations of m and d_{ae} distributions, respectively. m_c and $d_{ae,c}$
 194 are the geometric mean of m and d_{ae} , respectively.

195 The CPMA and AAC were calibrated with certified PSL spheres (Thermo, USA) with sizes of 70 nm, 150
 196 nm and 303 nm before the measurement. The measured m and d_{ae} were compared to m_{PSL} and $d_{ae,PSL}$, which
 197 were calculated with the nominal diameter and density of PSL (1050 kg m⁻³). The deviations between
 198 measured m and m_{PSL} or measured d_{ae} and $d_{ae,PSL}$ were 2.75% and 5.14%, respectively. To quantify the
 199 multiple charging effect of particles selected by the DMA-CPMA system, the soot particles were initially
 200 selected by the DMA-CPMA at different d_m and the corresponding m . Then, the d_{ae} distribution of mobility
 201 and mass selected particles was obtained by stepping the AAC rotation speed of the cylinder with
 202 simultaneous measurement of the particle concentration at the AAC outlet using a CPC (Fig. 1b).

203 **3 Results and discussion**

204 **3.1 Transfer function of the tandem system**

205 The DMA, PMA and AAC select particles based on the electrical mobility diameter, mass and aerodynamic
206 diameter, respectively. These properties can be connected as follows (Decarlo et al. 2004):

207
$$\frac{Cc(d_{ae})\rho_0 d_{ae}^2}{6} = \frac{Cc(d_m)\rho_{eff} d_m^2}{6} = m \frac{Cc(d_m)}{\pi d_m}, \quad (21)$$

208 where $\rho_{eff} = \frac{6m}{\pi d_m^3}$. The transfer function of the DMA-APM has been well documented and can be found in
209 Kuwata (2015). The convolution of the transfer functions of the DMA-CPMA and DMA-AAC were
210 calculated by the following equations.

211
$$\Phi_{DMA-CPMA} = \Omega_{CPMA}\Omega_{DMA}, \quad (22)$$

212
$$\Phi_{DMA-AAC} = \Omega_{DMA}\Omega_{AAC}, \quad (23)$$

213 where Φ and Ω are the transfer functions of the combined and individual classification systems expressed by
214 subscripts, respectively. In the following discussion, we explain the transfer functions of the DMA-CPMA
215 and DMA-AAC utilizing the literature data of soot particles (Pei et al., 2018). The d_m and m of the
216 representative particles are 100 nm and 0.33 fg, respectively, and the corresponding d_{ae} is 68.3 nm according
217 to Eq. (21). In the calculation, the following parameter set was employed: $d_m = 100$ nm, $Q_{DMA} = 0.3$ L min⁻¹,
218 $\beta_{DMA} = 0.1$, $m = 0.33$ fg, $Q_{CPMA} = 0.3$ L min⁻¹, $R_m = 8$, $d_{ae} = 68.3$ nm, $Q_{AAC} = 0.3$ L min⁻¹, $\beta_{AAC} = 0.1$. The
219 transfer functions of DMA-CPMA and DMA-AAC were solved iteratively using logarithmically spaced d_m ,
220 m and d_{ae} , which included 600 points each. The ranges of d_m , m and d_{ae} used in the calculations were from
221 0.8 times of $d_{m1,min}$ to 1.2 times of $d_{m2,max}$, and from 0.8 times of $m_{1,min}$ to 1.2 times of $m_{2,max}$, from 0.8 times
222 of $d_{ae,min}$ to 1.2 times of $d_{ae,max}$, respectively. The dimensions of the individual classifiers are summarized in
223 Table 1.

224 **DMA-CPMA**

225 The DMA-CPMA transfer function ($\Phi_{DMA-CPMA}$) for particles mentioned above, i.e., particles with d_m of 100
226 nm and m of 0.33 fg, is calculated in $\log(d_m)$ - $\log(m)$ space, as shown in Fig. 2. The particles are shown in
227 Fig. 2 in actual d_m and m , but when we calculate the resolution of DMA and CPMA, the mobility and effective
228 mass are used. The resolution of CPMA can be calculated by Eq. (15), where m_1 is the mass of singly charged
229 particles which can be selected by the CPMA, i.e., effective mass. In $\log(d_m)$ - $\log(m)$ space, the mass–mobility
230 relationship is

231
$$(m/\text{fg}) = k_f (d_m/\text{nm})^{D_{fm}}, \quad (24)$$

232
$$\log(m/\text{fg}) = D_{fm} \log(d_m/\text{nm}) + \log(k_f), \quad (25)$$

233 In general, D_{fm} equals 3 for spherical particles and smaller than 3 for aspherical particles, although D_{fm} can
234 be larger than 3 for particles that are non-spherical at small d_m and approach spherical as d_m increases. In the
235 $\log(d_m)$ - $\log(m)$ space, the relationship of m and d_m is linear, with the slope expressed as the mass–mobility
236 exponent (D_{fm}) and the intercept representing the pre-exponential factor (k_f). Under this specific operation
237 condition, no overlap was observed between the spherical particle population (black line) and the

238 classification region (the colored blocks) for doubly charged particles, implying that only the singly charged
 239 particles were selected. For aspherical particles with $D_{fm} < 3$, such as soot particles with aggregate structures,
 240 the particle population may overlap the doubly charged region when the slope (D_{fm}) is small enough; however,
 241 the combination of DMA and CPMA is generally used to avoid the multiple charge effect in soot studies.
 242 The reported D_{fm} values are typically in the range of 2.2–2.4 for fresh soot particles (Rissler et al., 2013) and
 243 diesel soot particles (Park et al., 2003). In the exemplary case (Pei et al., 2018), the derived D_{fm} of premixed
 244 flame-generated soot particles was 2.28, resulting in the particles population always going through the
 245 transfer area of doubly charged particles. This implies that the performance of the DMA-CPMA to eliminate
 246 multiply charged particles to a certain extent depends on the particle morphology.
 247 The DMA-CPMA system can eliminate the multiply charged particles only if the D_{fm} of the particles is larger
 248 than the slope of a line connecting $(d_m, m) = (d_{m2,min}, m_{2,max})(d_{m1}, m_1)$ (as PP_0 shown in Fig. 2). Since the
 249 CPMA is used downstream of the DMA, $m_{2,max}$ at the d_m of $d_{m2,min}$ can be calculated using Eq. (16) with the
 250 known mobility. Accordingly, the ideal condition under static operation to completely eliminate the multiply
 251 charged particles is

$$252 \quad D_{fm} > PP_0 = \frac{\log(m_{2,max}/m_1)}{\log(d_{m2,min}/d_{m1})} = \frac{\log\left(2 + \frac{2}{R_m(1+\beta_{DMA})}\right)}{\log\left(\frac{2}{(1+\beta_{DMA})} \frac{Cc(d_{m2,min})}{Cc(d_{m1})}\right)} \quad (26)$$

253 The ability of the DMA-CPMA to eliminate multiply charged particles depends on the selected d_m , m and
 254 resolutions of both the DMA and CPMA. Combining Eq. (15), equation (26) gives instructions in actual
 255 operation to eliminate multiply charged particles. When selecting particles of certain d_m and m , by decreasing
 256 Q_{CPMA} , or increasing ω and β_{DMA} , i.e., by increasing the resolution of the measurement, the potential of
 257 multiply charged particles is reduced. Thus, the key to evaluating whether there is a multiple charging effect
 258 lies in the particle morphology (D_{fm}) and the slope of PP_0 calculated from Eq. (26) theoretically.

259 In addition to the instrument setup, the particle morphology is also crucial for the DMA-CPMA. Here, we
 260 simulate the critical slope of PP_0 when selecting different d_m and m under the common selecting conditions
 261 ($\beta_{DMA} = 0.1$, $Q_{CPMA} = 0.3 \text{ L min}^{-1}$, $R_m = 8$) using Eq. (26), which is represented as contour lines in Fig. 3 (A
 262 black and white version is shown as Fig. S4). Under these selection conditions, the DMA-CPMA can select
 263 monodispersed particles when the D_{fm} of the particles is larger than the critical slope of PP_0 . When selecting
 264 small aspherical particles or particles with extremely low density, the critical slope of PP_0 is relatively higher,
 265 and the DMA-CPMA classification is sensitive to multiple charging effect. As shown in Fig. 3, d_m , m and
 266 the corresponding D_{fm} were taken from the literature (Park et al., 2003; Rissler et al., 2013; Tavakoli et al.,
 267 2014; Ait Ali Yahia et al., 2017; Dastanpour et al., 2017; Forestieri et al., 2018; Pei et al., 2018;
 268 Kazemimanesh et al., 2019a). Generally, for soot particles with D_{fm} of 2.2-2.4, the multiple charging effect
 269 can be avoided for the DMA-CPMA when selecting soot particles with mobility diameters larger than 200
 270 nm, while it fails to eliminate multiply charged particles when selecting small soot particles, as shown by the
 271 circles and squares in Fig. 3. These potential uncertainties are discussed in detail with flame-generated soot
 272 particles in Sect. 3.2.

273 DMA-AAC

274 The advantage of the AAC versus the CPMA is that there is no need for a neutralizer to charge aerosol
 275 particles to a known charge state. Measuring solely with an AAC will avoid multiple charging. However,
 276 aspherical particles with different mass can be selected by the AAC as having identical aerodynamic diameter
 277 (Kazemimanesh et al., 2022). According to Eq. (21), the population selected by AAC has one physical size
 278 (d_{ae}) but the d_m range of this population is wide since soot particles have different densities. Multiple charging
 279 becomes a problem when the tandem measurement is made with a DMA or PMA. According to Eq. (21) and
 280 Eq. (24), the relationship of d_{ae} and d_m of aspherical particles can be expressed as follows:

$$281 \log(d_{ae}/nm) = \frac{1}{2}(D_{fm} - 1)\log(d_m/nm) + \frac{1}{2}\log\left(\frac{6}{\pi} \frac{Cc(d_m)k_f}{Cc(d_{ae})\rho_0} \cdot 10^9\right), \quad (27)$$

282 which indicates that the relationship between d_{ae} and d_m is nonlinear since $Cc(d_m)$ and $Cc(d_{ae})$ vary with d_m
 283 and d_{ae} , respectively. Particle morphology can be derived from the relationship between d_m and d_{ae} measured
 284 by a DMA and AAC, respectively. To simulate the transfer function of the DMA-AAC, the same particles
 285 ($d_m = 100$ nm, $m = 0.33$ fg, $D_{fm} = 2.28$) as those used in the calculations of the DMA-CPMA were selected.
 286 The corresponding d_{ae} was numerically solved using the known mass-mobility relationship. The transfer
 287 function of the DMA-AAC is shown in $\log(d_{ae})$ - $\log(d_m)$ (Fig. 4a). In the transfer function of DMA-CPMA,
 288 the classification regions of singly charged particles and doubly charged particles are on the diagonal. The
 289 oblique line of particles population is more likely to go through the region of doubly charged particles in the
 290 transfer function of DMA-CPMA. The transfer functions of singly charged and doubly charged particles are
 291 in parallel for the DMA-AAC, suggesting that the particles population is less likely to overlap with the region
 292 of multiply charged particles. Using the example setups ($d_m = 100$ nm, $Q_{DMA} = 0.3$ L min⁻¹, $\beta_{DMA} = 0.1$, $d_{ae} =$
 293 68.3 nm, $Q_{AAC} = 0.3$ L min⁻¹, $\beta_{AAC} = 0.1$) of the DMA-AAC, truly monodispersed particles are selected for
 294 spherical particles and typical soot particles.

295 Similar to the DMA-CPMA system, eliminating multiply charged particles requires that the $d_{ae,max}$ of the
 296 AAC at $d_{m2,min}$ must be smaller than the d_{ae} of particles of interest, which can be derived from $d_{m2,min}$ and D_{fm}
 297 (Eq. (27)),

$$298 d_{ae}(d_{m2,min}, D_{fm}) > d_{ae,max}(d_{m2,min}),$$

$$299 \Rightarrow D_{fm} > \frac{\log(2^{\frac{1+\beta_{AAC}}{1+\beta_{DMA}}})}{\log\left[\frac{2}{1+\beta_{DMA}} \frac{Cc(d_{m2,min})}{Cc(d_{m1})}\right]}, \quad (28)$$

300 This equation describes the minimum value of D_{fm} to eliminate the multiple charging effect. It is clearly
 301 shown that the mobility resolution of the DMA and the relaxation time resolution of the AAC determine the
 302 limiting condition, and the resolution of the AAC is more important compared with the resolution of the
 303 DMA. The limiting condition is also related to the selected d_m of the DMA but independent of the selected
 304 d_{ae} of the AAC (Fig. S1). Setting the same resolutions for the DMA and AAC, particle selection is more
 305 susceptible to multiple charging effects when selecting small sizes. In Fig. 4a, the values of β_{DMA} and β_{AAC}
 306 are 0.1, resulting in a minimum D_{fm} of 1.41. This D_{fm} is smaller than that for most aerosols. Hence, the
 307 selected particles of the DMA-AAC are truly monodisperse regardless of the particle morphology. However,
 308 in actual operations, a larger sample flow rate may be required to satisfy the apparatus downstream, while

309 the maximum sheath flow rate of the classifier is restricted by the instrument design (e.g., 30 L min⁻¹ for the
310 DMA and 15 L min⁻¹ for the AAC). In addition, the maximum size ranges are also restricted by the sheath
311 flow, so in some cases, a lower sheath flow rate is required to select larger particles. When increasing β_{AAC}
312 to 0.3 (decreasing the resolution of AAC) and leaving β_{DMA} unchanged, the transfer function becomes broader
313 (Fig. 4b). The minimum D_{fm} is 2.44, which indicates that the multiple charging effect exists for typical soot
314 particles with D_{fm} of 2.2-2.4. The line representing soot particles overlaps with the region of doubly charged
315 particles. Thus, reducing the resolutions of the DMA or AAC is not suggested in actual operations.

316 We think the transfer functions of DMA-AAC or AAC-DMA are identical regardless of the order of DMA
317 and AAC. For example, we use AAC-DMA to select particles with d_{ae} of 68 nm and d_{m} of 100 nm. In Fig.
318 4a, the transfer function of AAC is the region between the horizontal lines of $d_{\text{ae,max}}$ (75 nm) and $d_{\text{ae,min}}$ (63
319 nm). The soot particles population (red line) goes through this region will be selected by AAC. The mobility
320 diameter distribution of these relaxation time selected particles is around 80 nm to 120 nm. Then the DMA
321 is fixed to select particles with d_{m} of 100 nm, the particles with double charges and the same mobility (d_{m} of
322 150 nm) have been excluded by AAC. As a result, AAC-DMA select monodispersed particles with d_{ae} of
323 68.3 nm and d_{m} of 100 nm. In Fig. 4b, the resolution of AAC is lower and transfer function of AAC is broader
324 than that in Fig. 4a. The soot particles population (red line) goes through the transfer function region between
325 the horizontal lines at d_{ae} of $d_{\text{ae,max}}$ (50 nm) and $d_{\text{ae,min}}$ (86 nm). The mobility diameter distribution of these
326 relaxation time selected particles is very wide from less than 80 nm to about 158 nm. Then these relaxation
327 time selected particles were charged and selected by DMA at d_{m} of 100 nm, singly charged particles with d_{m}
328 of 95 nm~106 nm and doubly charged particles with d_{m} of 142 nm~158 nm will be selected.

329 If we use the DMA-AAC, the particles are selected by DMA first. For example, in Fig. 4b, the transfer
330 function of DMA is shown as two vertical regions which particles with single and double charges can
331 penetrate. The soot particles (red line) goes through it and two populations of soot particles with mode d_{m} of
332 100 nm and 150 nm will be selected. The corresponding d_{ae} distributions of these singly and doubly charged
333 particles are 66 nm~70 nm and 81 nm~87 nm. These mobility-selected particles are selected at d_{ae} of 68.3
334 nm by AAC and the transfer function of AAC shows that particles with d_{ae} of 50 nm~86 nm can penetrate.
335 As a result, singly charged particles with d_{ae} of 66 nm ~70 nm and doubly charged particles with d_{ae} of 81
336 nm ~86 nm can be selected.

337 As a summary, the transfer functions of DMA-AAC and AAC-DMA in a static configuration are the same
338 no matter the ordering of DMA and AAC.

339 **3.2 Evaluation of the multiple charging effect**

340 To quantify the possible biases of the multiple charging effect in the DMA-CPMA system, we conducted a
341 soot experiment, as demonstrated in Fig. 1. For each mobility-selected particles, the distributions of number
342 density as a function of d_{ae} and m were determined by the scans. These distributions were then fit to a log-
343 normal to determine the modal values ($d_{\text{ae,c}}$, m_{c}) and from these values the ρ_{eff} were determined. The
344 uncertainties of $d_{\text{ae,c}}$ and m_{c} were standard deviation of multiple measurements. Representative plots for the

345 measured distributions of m and d_{ae} of particles with d_m of 150 nm and 250 nm are shown in Fig. S2. The
 346 results are summarized in Table 2. The fitted values of D_{fm} and k_f were 2.28 and 7.49×10^{-6} fg, respectively,
 347 indicating a fractal structure, which is the same as in previous studies (Pei et al., 2018). The effective densities
 348 of generated soot particles vary from $>500 \text{ kg m}^{-3}$ at $d_m = 80 \text{ nm}$ to $<300 \text{ kg m}^{-3}$ at d_m of 250 nm determined
 349 by DMA-CPMA and DMA-AAC. In general, the deviation of values of ρ_{eff} measured by DMA-CPMA and
 350 DMA-AAC monotonically decreases with increasing particle size. The deviation is 7.65% for particles of 80
 351 nm, whereas it decreased to $<1\%$ for particles larger than 200 nm. The results reveal a strict agreement
 352 between the two methods for retrieving the particle effective density.

353 According to Fig. 3, the critical slopes of PP_0 for soot particles with d_m of 80 nm, 100 nm, 150 nm, 200 nm
 354 and 250 nm are 2.46, 2.41, 2.29, 2.17 and 2.08, respectively. The measured D_{fm} of 2.28 is smaller than the
 355 calculated PP_0 for particles with d_m smaller than 200 nm, which suggests that the contributions from the
 356 multiply charged particles cannot be eliminated.

357 When selecting particles with d_m of 80 nm and m of 0.16 fg, the corresponding DMA-CPMA transfer function
 358 is shown in Fig. 5a. DMA-CPMA is set to select singly charged particles with d_m of 80 nm and m of 0.16 fg,
 359 while the doubly charged particles with d_m of 119.3 nm and m of 0.32 fg will also be selected and the transfer
 360 function is presented as upper right region. Soot particles curve (red line) goes through the upper-right region
 361 which doubly charged particle can penetrate (d_m of 113 nm~118 nm, m of 0.35 fg~0.39 fg). As a result, we
 362 conclude that multiple charging effect still exists when DMA-CPMA select soot particles with d_m of 80 nm
 363 and m of 0.16 fg. Since the classification of the AAC is different from the DMA and CPMA, the aerodynamic
 364 size distributions of mobility- and mass- selected particles were characterized. Fig. 5b shows the particles
 365 number density aerodynamic size distribution ($PNSD_{ae}$) scanned by the AAC. For each measurement,
 366 $PNSD_{ae}$ was fitted using log-normal distributions, and three peaks corresponding to singly, doubly and triply
 367 charged particles were identified. The fractional number concentration of particles with different charging
 368 state is expressed as follows,

$$369 \quad f_{N,n} = \frac{\int_{d_{ae,low}}^{d_{ae,high}} \frac{dN_n}{d \log(d_{ae})} d \log(d_{ae})}{\sum_{n=1}^3 \int_{d_{ae,low}}^{d_{ae,high}} \frac{dN_n}{d \log(d_{ae})} d \log(d_{ae})}, \quad (29)$$

370 where $f_{N,n}$ and N_n are the fractional number concentration and number concentration of particles bearing n
 371 charges. $d_{ae,low}$ and $d_{ae,high}$ denote the minimum and maximum values of d_{ae} scanned by AAC, respectively.
 372 The uncertainties are standard deviations of multiple measurements. Some small particles remaining in the
 373 AAC induced the peak at $d_{ae} < 40 \text{ nm}$. These residual particles were measured even if the sample flow was
 374 filtered. For particles with $d_m = 80 \text{ nm}$, the modal d_{ae} values were 53.9 nm, 60.6 nm and 70.9 nm, and the
 375 corresponding d_{ae} values were calculated as 51.5 nm, 62.0 nm and 70.7 nm using Eq. (1) and Eq. (17). The
 376 experimental results are consistent with the theoretical results with deviations within 5.3%.

377 When selecting particles with d_m of 200 nm and m of 1.28 fg, the transfer function is shown in Fig. 6a. The
 378 PP_0 slope of 2.17 is smaller than that D_{fm} of 2.28, and the generated particles population does not overlap
 379 with the block of doubly charged particles; thus, the DMA-CPMA classified particles were truly

380 monodispersed. PNSD_{ae} measured by the AAC is unimodal, implying that the classified particles were singly
381 charged (Fig. 6b).

382 The results of other experiments are shown in Fig. S3. Although the critical slope of PP_0 when selecting 150
383 nm particles is close to D_{fm} and the transfer function of DMA-CPMA also showed that negligible multiply
384 charged particles would be selected (Fig. S3d), doubly charged particles were measured in PNSD_{ae} (Fig. S3e).
385 These doubly charged particles were selected, probably owing to particle diffusion. The nondiffusion models
386 were used to calculate the transfer function, but the transfer function can be broader because of diffusion. In
387 summary, for a type of particle with the same mass–mobility relationship, the possibility of multiple charging
388 increases for small particles when selected by the DMA-CPMA system, which is consistent with the
389 theoretical calculation in Sect. 3.1.

390 3.3 Atmospheric implication

391 The DMA-APM and DMA-CPMA systems are usually adopted to eliminate multiply charged particles in
392 soot aerosol studies. Although they might fail to select monodispersed particles, downstream measurements
393 by instruments such as a single-particle soot photometer (SP2) will not be interfered with, which characterizes
394 the distinct information of a single particle. Nevertheless, for techniques measuring the properties of an entire
395 aerosol population, e.g., scattering coefficient by a nephelometer or absorption coefficient by a photoacoustic
396 spectrometer, multiply charged particles can induce significant bias. A previous study (Radney and
397 Zangmeister, 2016) noted that the DMA-APM failed to resolve multiply charged particles for soot particles
398 when selecting 150 nm flame-generated particles, which caused a 110% error in extinction measurement. To
399 investigate the multiple charging effect for DMA-CPMA classification, the optical absorption coefficient of
400 particles with different charging states after DMA-CPMA classification was calculated from PNSD_{ae} . Mie
401 theory was used to calculate the theoretical absorption coefficient at a wavelength of 550 nm. Mie theory is
402 probably not the “best” method to use here since soot particles are aspherical agglomerates. Realistically,
403 however, the Mie comparison is only being used to prove a point about the impact of multiple charging.
404 Therefore, in this instance, any errors in the calculated optical properties are somewhat inconsequential. The
405 refractive index used in the Mie code was $1.95+0.79i$ (Bond and Bergstrom, 2006). The PNSD_{ae} for different
406 charging state particles was converted to volume-equivalent diameter size distributions (PNSD_{ve}), which was
407 used in Mie theory to determine the absorption coefficient. The method to calculate PNSD_{ve} is described in
408 Sect. S1. Subsequently, the absorption coefficient, α_{abs} , was derived using Mie theory and the PNSD_{ve} of
409 particles with different charging states. The fractional absorption coefficient for particles with different
410 charging state is calculated as follows,

$$411 \quad f_{\text{abs},n} = \frac{\int_{d_{\text{ve},\text{low},n}}^{d_{\text{ve},\text{high},n}} \frac{d\alpha_{\text{abs},n}}{d\log(d_{\text{ve}})} d\log(d_{\text{ve}})}{\sum_{i=1}^3 \int_{d_{\text{ve},\text{low},n}}^{d_{\text{ve},\text{high},n}} \frac{dN_n}{d\log(d_{\text{ve}})} d\log(d_{\text{ve}})}, \quad (30)$$

412 where $f_{\text{abs},n}$ and $\alpha_{\text{abs},n}$ are the fractional absorption coefficient and absorption coefficient of particles bearing
413 n charges, respectively. $d_{\text{ve},\text{low},n}$ and $d_{\text{ve},\text{high},n}$ denote the minimum and maximum value of d_{ve} of particles with
414 n charges, which are converted from $d_{\text{ae},\text{low}}$ and $d_{\text{ae},\text{high}}$ scanned by AAC, respectively.

415 The overestimation of mass absorption cross-section (MAC) is calculated by

$$416 \frac{\Delta \text{MAC}}{\text{MAC}} = \frac{\frac{\alpha_{\text{abs,tot}}}{m_p N_{\text{tot}}} \frac{f_{\text{abs},1} \alpha_{\text{abs,tot}}}{m_p f_{N,1} N_{\text{tot}}}}{\frac{f_{\text{abs},1} \alpha_{\text{abs,tot}}}{m_p f_{N,1} N_{\text{tot}}}} = \frac{f_{N,1}}{f_{\text{abs},1}} - 1, \quad (31)$$

417 where $\alpha_{\text{abs,tot}}$ and N_{tot} is the total absorption coefficient and number concentration of particles selected by
418 DMA-CPMA, respectively. m_p is the actual mass of singly charged particles selected by DMA-CPMA. The
419 uncertainties were calculated from propagation of errors. For soot particles with diameters <200 nm, the
420 optical absorption contributions of particles with different charging states and the MAC overestimation are
421 summarized in Table 3. For soot particles with a diameter of 80 nm, the contributions of particles with
422 different charging states are shown in Fig. 5c. Doubly charged particles only account for 26.7% \pm 3.0% of the
423 total number concentration but provide a large fractional contribution to the total absorption (45.7% \pm 4.2%).
424 Additionally, a small fraction (1.1% \pm 0.4%) of triply charged particles accounted for 3.7% \pm 1.5% of the
425 absorption. As a result, the MAC was overestimated by 42.7% \pm 9.1%, and the directive radiative force (DRF)
426 was overestimated by 42.7% \pm 9.1%. The DRF was calculated using previous global climate models (Bond et
427 al., 2016). For particles selected by the DMA-CPMA at a d_m of 200 nm and an m of 1.28 fg, the selected
428 particles were truly dispersed, and the measured optical properties were valid (Fig. 6c).

429 A large amount of 70 nm -90 nm soot particles was emitted from diesel engine (Wierzbicka et al., 2014), and
430 neglecting the multiple charging effect in the measurement of mass-specific MAC on this size range will
431 result in significant bias in the estimation of radiative forcing of automobile-emitted soot particles, which
432 may lead to large errors in climate model.

433 According to Table 3, the number fraction of doubly charged particles declines with the size of the nominated
434 particles, i.e., 26.7% \pm 3.0% and 17.6% \pm 0.5% for 80 nm and 100 nm particles, respectively, but only 4.2% \pm 1.1%
435 for 150 nm particles. Accordingly, the MAC was largely overestimated for 80 nm and 100 nm particles
436 (42.7% \pm 9.1% and 28.0% \pm 1.8%, respectively) but moderately overestimated for 150 nm particles
437 (9.2% \pm 4.1%). To summarize, our results indicated that the combination of tandem classifiers is not sufficient
438 to completely eliminate multiply charged particles when selecting small flame-generated soot particles,
439 which introduced noticeable bias for absorption measurements and led to overestimation of the MAC. As a
440 result, the DRF of soot particles was also overestimated.

441 **4 Conclusion**

442 In this study, we demonstrate the transfer functions of DMA-CPMA and DMA-AAC and discuss their
443 limitations to eliminate multiply charged particles. For aspherical particles, there is no guarantee that the
444 multiple charging effect can be avoided in DMA-CPMA or DMA-AAC systems. Usually, a DMA-AAC can
445 select truly monodisperse particles, but the method can suffer from multiple charging when decreasing the
446 resolutions of the DMA and AAC. The ability of the DMA-CPMA to eliminate multiple charging effect
447 mainly depends on the particle morphology and the instrument resolutions. This tandem system is more
448 sensitive to multiple charging effect with decreasing D_{fm} and decreasing nominal size of particles. The DMA-

449 CPMA failed to eliminate multiply charged particles when selecting soot particles with diameters < 150 nm.
 450 Although doubly charged particles accounted for a small fraction of the number concentration, they
 451 contributed most significantly to light absorption, which indicated that multiply charged particles can induce
 452 an obvious contribution to light absorption and lead to an overestimation of DRF for flame-generated soot
 453 particles.

454

455 *Code/Data availability.* Code/Data are available upon request.

456 *Author contributions.* ZW determined the main goal of this study. YS and XP designed the methods. YS
 457 carried them out and prepared the paper with contributions from all coauthors. YS, HL and JZ analyzed the
 458 optical data.

459 *Competing interests.* The authors declare that they have no conflicts of interest.

460 *Acknowledgments.* The study was supported by the National Natural Science Foundation of China (91844301
 461 and 41805100). We especially acknowledge useful comments and suggestions on the MATLAB script of the
 462 CPMA transfer function from Timothy A. Sipkens.

463 **Appendix A**

464 **A1. Nomenclature**

Parameter	Definition
B	Mechanical mobility
$C_c(d_p)$	Cunningham slip correction factor
c_r	Particle migration velocity
d_{ae}	Aerodynamic equivalent diameter
$d_{ae,c}$	the geometric mean of d_{ae} distribution measured by AAC-CPC
$d_{ae,high}$	The maximum value of d_{ae} scanned by AAC
$d_{ae,low}$	The minimum value of d_{ae} scanned by AAC
$d_{ae,max}$	The maximum d_{ae} of particles that can be selected in AAC classification
$d_{ae,min}$	The minimum d_{ae} of particles that can be selected in AAC classification
d_m	Mobility equivalent diameter
$d_{mn,max}$	The maximum d_m of particles with n charges that can be selected in DMA classification
$d_{mn,min}$	The minimum d_m of particles with n charges that can be selected in DMA classification
d_{ve}	Volume-equivalence size
D_{fm}	Mass-mobility exponent
e	Elementary charge

$f_{N,n}$	The fractional number concentration of particles with n charges
$f_{\text{abs},n}$	The fractional absorption coefficient of particles with n charges
k_f	Mass-mobility pre-exponential factor
L	Length of DMA, CPMA or AAC
m	Particle mass
m_c	the geometric mean of m distribution measured by CPMA-CPC
$m_{n,\text{max}}$	The maximum m of particles with n charges that can be selected in CPMA classification
$m_{n,\text{min}}$	The minimum m of particles with n charges that can be selected in CPMA classification
n	Number of elementary charges on the particle
N_{tot}	The total number concentration of particles selected by DMA-CPMA
PNSD	Particle number size distribution
PNSD _{ae}	Particle number aerodynamic size distribution
PNSD _{ve}	Particle number volume-equivalent size distribution
q	Electrical charge on the particle
Q_a	Sample flow rate
Q_{sh}	Sheath flow rate
Q_{CPMA}	The volumetric flow rate in CPMA
r_a	Lower initial radial position that passes through the classifier
r_b	Upper initial radial position that passes through the classifier
r_1	Inner radius
r_2	Outer radius
\hat{r}	r_1 / r_2
R_m	Mass resolution of CPMA
t	Time
\bar{v}	Average flow velocity
v_z	Axial flow distribution
v_θ	Velocity profile in the angular direction
V	Voltage between the two electrodes of DMA or CPMA
Z_p	Electrical mobility
Z_p^*	Z_p at the maximum transfer function of DMA
\tilde{Z}_p	Z_p / Z_p^*
$\alpha \beta$	Azimuthal flow velocity distribution parameter
α_{abs}	Absorption coefficient
$\alpha_{\text{abs,tot}}$	The total absorption coefficient of particles selected by DMA-CPMA
β_{AAC}	The ratio of flow rates of aerosol flow and sheath flow of AAC

β_{DMA}	The ratio of flow rates of aerosol flow and sheath flow of DMA
δ	Half width of the gap between the two electrodes
μ	Air viscosity
ρ_0	Standard density, which equals 1 kg m^{-3}
ρ_{eff}	Effective density
σ_m	The geometric standard deviation of m distribution
σ_{ac}	The geometric standard deviation of d_{ac} distribution
τ	Relaxation time
τ^*	τ at the maximum of the transfer function
$\tilde{\tau}$	Dimensionless particle relaxation time, $\tilde{\tau} = \tau/\tau^*$
χ	The dynamic shape factor
ω_1	Rotational speed of the inner electrode
ω_2	Rotational speed of the outer electrode
$\hat{\omega}$	ω_1/ω_2
Ω	Transfer function

465 **References**

- 466 Ait Ali Yahia, L., Gehin, E., and Sagot, B.: Application of the Thermophoretic Annular Precipitator (TRAP)
467 for the study of soot aggregates morphological influence on their thermophoretic behaviour, *J. Aerosol Sci.*,
468 113, 40-51, <https://doi.org/10.1016/j.jaerosci.2017.07.018>, 2017.
- 469 Biskos, G., Malinowski, A., Russell, L. M., Buseck, P. R., and Martin, S. T.: Nanosize Effect on the
470 Deliquescence and the Efflorescence of Sodium Chloride Particles, *Aerosol Sci. Technol.*, 40, 97-106,
471 <https://doi.org/10.1080/02786820500484396>, 2006.
- 472 Bond, T. C., and Bergstrom, R. W.: Light Absorption by Carbonaceous Particles: An Investigative Review,
473 *Aerosol Sci. Technol.*, 40, 27-67, <https://doi.org/10.1080/02786820500421521>, 2006.
- 474 Bond, T. C., Doherty, S. J., Fahey, D. W., Forster, P. M., Berntsen, T., DeAngelo, B. J., Flanner, M. G., Ghan,
475 S., Köhler, B., Koch, D., Kinne, S., Kondo, Y., Quinn, P. K., Sarofim, M. C., Schultz, M. G., Schulz, M.,
476 Venkataraman, C., Zhang, H., Zhang, S., Bellouin, N., Guttikunda, S. K., Hopke, P. K., Jacobson, M. Z.,
477 Kaiser, J. W., Klimont, Z., Lohmann, U., Schwarz, J. P., Shindell, D., Storelvmo, T., Warren, S. G., and
478 Zender, C. S.: Bounding the role of black carbon in the climate system: A scientific assessment, *J. Geophys.*
479 *Res.: Atmos.: Atmospheres*, 118, 5380-5552, <https://doi.org/10.1002/jgrd.50171>, 2013.
- 480 Cheng, Y., Su, H., Koop, T., Mikhailov, E., and Pöschl, U.: Size dependence of phase transitions in aerosol
481 nanoparticles, *Nat. Commun.*, 6, <https://doi.org/10.1038/ncomms6923>, 2015.
- 482 Dastanpour, R., Momenimovahed, A., Thomson, K., Olfert, J., and Rogak, S.: Variation of the optical
483 properties of soot as a function of particle mass, *Carbon*, 124, 201-211,
484 <https://doi.org/10.1016/j.carbon.2017.07.005>, 2017.

485 Dusek, U., Frank, G. P., Hildebrandt, L., Curtius, J., Schneider, J., Walter, S., Chand, D., Drewnick, F., Hings,
486 S., Jung, D., Borrmann, S., and Andreae, M. O.: Size Matters More Than Chemistry for Cloud-Nucleating
487 Ability of Aerosol Particles, *Science*, 312, 1375-1378, <https://doi.org/10.1126/science.1125261>, 2006.

488 Ehara, K., Hagwood, C., and Coakley, K. J.: Novel method to classify aerosol particles according to their
489 mass-to-charge ratio—Aerosol particle mass analyser, *J. Aerosol Sci*, 27, 217-234,
490 [https://doi.org/10.1016/0021-8502\(95\)00562-5](https://doi.org/10.1016/0021-8502(95)00562-5), 1996.

491 Johnson, T. J.; Nishida, R. T.; Zhang, X.; Symonds, J. P. R.; Olfert, J. S.; Boies, A. M., Generating an aerosol
492 of homogeneous, non-spherical particles and measuring their bipolar charge distribution. *J. Aerosol Sci*, 153.
493 <https://doi.org/10.1016/j.jaerosci.2020.105705>, 2021.

494 Johnson, T. J.; Olfert, J. S.; Cabot, R.; Treacy, C.; Yurteri, C. U.; Dickens, C.; McAughey, J.; Symonds, J. P.
495 R., Steady-state measurement of the effective particle density of cigarette smoke. *J. Aerosol Sci*, 75, 9-16,
496 <https://doi.org/10.1016/j.jaerosci.2014.04.006>, 2014.

497 Kazemimanesh, M., Dastanpour, R., Baldelli, A., Moallemi, A., Thomson, K. A., Jefferson, M. A., Johnson,
498 M. R., Rogak, S. N., and Olfert, J. S.: Size, effective density, morphology, and nano-structure of soot particles
499 generated from buoyant turbulent diffusion flames, *J. Aerosol Sci.*, 132, 22-31,
500 <https://doi.org/10.1016/j.jaerosci.2019.03.005>, 2019a.

501 Kazemimanesh, M., Moallemi, A., Thomson, K., Smallwood, G., Lobo, P. and Olfert, J.S.: A novel miniature
502 inverted-flame burner for the generation of soot nanoparticles. *Aerosol Sci. and Technol.*, 53(2), 184-195,
503 <https://doi.org/10.1080/02786826.2018.1556774>, 2019b.

504 Kazemimanesh, M., Rahman, M.M., Duca, D., Johnson, T.J., Addad, A., Giannopoulos, G., Focsa, C. and
505 Boies, A.M.: A comparative study on effective density, shape factor, and volatile mixing of non-spherical
506 particles using tandem aerodynamic diameter, mobility diameter, and mass measurements. *J. Aerosol Sci.*,
507 161, 105930, <https://doi.org/10.1016/j.jaerosci.2021.105930>, 2022.

508 Knutson, E. O., and Whitby, K. T.: Aerosol classification by electric mobility: apparatus, theory, and
509 applications, *J. Aerosol Sci.*, 6, 443-451, [https://doi.org/10.1016/0021-8502\(75\)90060-9](https://doi.org/10.1016/0021-8502(75)90060-9), 1975.

510 Kuwata, M.: Particle Classification by the Tandem Differential Mobility Analyzer–Particle Mass Analyzer
511 System, *Aerosol Sci. Technol.*, 49, 508-520, <https://doi.org/10.1080/02786826.2015.1045058>, 2015.

512 Moallemi, A.; Kazemimanesh, M.; Corbin, J. C.; Thomson, K.; Smallwood, G.; Olfert, J. S.; Lobo, P.,
513 Characterization of black carbon particles generated by a propane-fueled miniature inverted soot generator.
514 *J. Aerosol Sci.*, 135, 46-57, <https://doi.org/10.1016/j.jaerosci.2019.05.004>, 2019.

515 Olfert, J. S., and Collings, N.: New method for particle mass classification—the Couette centrifugal particle
516 mass analyzer, *J. Aerosol Sci.*, 36, 1338-1352, <https://doi.org/10.1016/j.jaerosci.2005.03.006>, 2005.

517 Park, K., Cao, F., Kittelson, D. B., and McMurry, P. H.: Relationship between Particle Mass and Mobility for
518 Diesel Exhaust Particles, *Environ. Sci. & Technol.*, 37, 577-583, <https://doi.org/10.1021/es025960v>, 2003.

519 Park, K., Dutcher, D., Emery, M., Pagels, J., Sakurai, H., Scheckman, J., Qian, S., Stolzenburg, M. R., Wang,
520 X., Yang J., and McMurry P. H.: Tandem Measurements of Aerosol Properties—A Review of Mobility

521 Techniques with Extensions. *Aerosol Sci. and Technol.*, 42, 801-816,
522 <https://doi.org/10.1080/02786820802339561>, 2008.

523 Pei, X., Hallquist, M., Eriksson, A. C., Pagels, J., Donahue, N. M., Mentel, T., Svenningsson, B., Brune, W.,
524 and Pathak, R. K.: Morphological transformation of soot: investigation of microphysical processes during
525 the condensation of sulfuric acid and limonene ozonolysis product vapors, *Atmos. Chem. Phys.*, 18, 9845-
526 9860, <https://doi.org/10.5194/acp-18-9845-2018>, 2018.

527 Radney, J. G., Ma, X., Gillis, K. A., Zachariah, M. R., Hodges, J. T., and Zangmeister, C. D.: Direct
528 Measurements of Mass-Specific Optical Cross Sections of Single-Component Aerosol Mixtures, *Anal.*
529 *Chem.*, 85, 8319-8325, <https://doi.org/10.1021/ac401645y>, 2013.

530 Radney, J. G., and Zangmeister, C. D.: Practical limitations of aerosol separation by a tandem differential
531 mobility analyzer–aerosol particle mass analyzer, *Aerosol Sci. Technol.*, 50, 160-172,
532 <https://doi.org/10.1080/02786826.2015.1136733>, 2016.

533 Rissler, J., Messing, M. E., Malik, A. I., Nilsson, P. T., Nordin, E. Z., Bohgard, M., Sanati, M., and Pagels,
534 J. H.: Effective Density Characterization of Soot Agglomerates from Various Sources and Comparison to
535 Aggregation Theory, *Aerosol Sci. Technol.*, 47, 792-805, [10.1080/02786826.2013.791381](https://doi.org/10.1080/02786826.2013.791381), 2013.

536 Shiraiwa, M., Kondo, Y., Iwamoto, T., and Kita, K.: Amplification of Light Absorption of Black Carbon by
537 Organic Coating, *Aerosol Sci. & Technol.*, 44, 46-54, <https://doi.org/10.1080/02786820903357686>, 2010.

538 Sipkens, T. A., Olfert, J. S., and Rogak, S. N.: New approaches to calculate the transfer function of particle
539 mass analyzers, *Aerosol Sci. Technol.*, 54, 111-127, <https://doi.org/10.1080/02786826.2019.1680794>, 2019.

540 Stolzenburg, M. R., and McMurry, P. H.: Equations Governing Single and Tandem DMA Configurations
541 and a New Lognormal Approximation to the Transfer Function, *Aerosol Sci. Technol.*, 42, 421-432,
542 <https://doi.org/10.1080/02786820802157823>, 2008.

543 Swietlicki, E., Hansson, H. C., Hämeri, K., Svenningsson, B., Massling, A., McFiggans, G., McMurry, P. H.,
544 Petäjä T., Tunved, P., Gysel, M., Topping, D., Weingartner, E., Baltensperger, U., Rissler, J., Wiedensohler,
545 A., and Kulmala, M.: Hygroscopic properties of submicrometer atmospheric aerosol particles measured with
546 H-TDMA instruments in various environments – a review, *Tellus B*, 60, 432–469,
547 <https://doi.org/10.1111/j.1600-0889.2008.00350.x>, 2008.

548 Tavakoli, F., and Olfert, J. S.: An Instrument for the Classification of Aerosols by Particle Relaxation Time:
549 Theoretical Models of the Aerodynamic Aerosol Classifier, *Aerosol Sci. Technol.*, 47, 916-926,
550 <https://doi.org/10.1080/02786826.2013.802761>, 2013.

551 Tavakoli, F., and Olfert, J. S.: Determination of particle mass, effective density, mass–mobility exponent,
552 and dynamic shape factor using an aerodynamic aerosol classifier and a differential mobility analyzer in
553 tandem, *J. Aerosol Sci.*, 75, 35-42, <https://doi.org/10.1016/j.jaerosci.2014.04.010>, 2014.

554 Wiedensohler, A., Birmili, W., Nowak, A., Sonntag, A., Weinhold, K., Merkel, M., Wehner, B., Tuch, T.,
555 Pfeifer, S., Fiebig, M., Fjåraa, A. M., Asmi, E., Sellegri, K., Depuy, R., Venzac, H., Villani, P., Laj, P., Aalto,
556 P., Ogren, J. A., Swietlicki, E., Williams, P., Roldin, P., Quincey, P., Hüglin, C., Fierz-Schmidhauser, R.,
557 Gysel, M., Weingartner, E., Riccobono, F., Santos, S., Gröning, C., Faloon, K., Beddows, D., Harrison, R.,

558 Monahan, C., Jennings, S. G., O'Dowd, C. D., Marinoni, A., Horn, H.-G., Keck, L., Jiang, J., Scheckman, J.,
559 McMurry, P. H., Deng, Z., Zhao, C. S., Moerman, M., Henzing, B., de Leeuw, G., Lösschau, G., and Bastian,
560 S.: Mobility particle size spectrometers: harmonization of technical standards and data structure to facilitate
561 high quality long-term observations of atmospheric particle number size distributions, *Atmos. Meas. Tech.*,
562 5, 657–685, <https://doi.org/10.5194/amt-5-657-2012>, 2012.

563 Yao, Q., Asa-Awuku, A., Zangmeister, C. D., and Radney, J. G.: Comparison of three essential sub-
564 micrometer aerosol measurements: Mass, size and shape, *Aerosol Sci. Technol.*, 1-18,
565 <https://doi.org/10.1080/02786826.2020.1763248>, 2020.

566 Zangmeister, C. D., You, R., Lunny, E. M., Jacobson, A. E., Okumura, M., Zachariah, M. R., and Radney, J.
567 G.: Measured in-situ mass absorption spectra for nine forms of highly-absorbing carbonaceous aerosol,
568 *Carbon*, 136, 85-93, <https://doi.org/10.1016/j.carbon.2018.04.057>, 2018.

569 Zhang, R., Khalizov, A. F., Pagels, J., Zhang, D., Xue, H., and McMurry, P. H.: Variability in morphology,
570 hygroscopicity, and optical properties of soot aerosols during atmospheric processing, *Proc. Natl. Acad. Sci.*,
571 105, 10291, <https://doi.org/10.1073/pnas.0804860105>, 2008.

572

573

Table 1 Dimensions of the three classifiers used for transfer function calculation

Parameter	DMA	CPMA	AAC
r_1 (mm)	9.37	100	43
r_2 (mm)	19.61	103	45
L (mm)	44.369	200	210
ω_2/ω_1	—	0.945	—

574

Table 2. Mobility diameter, mass, aerodynamic diameter, effective densities calculated by DMA-AAC and DMA-CPMA, and the deviation between them for fresh soot particles in the size range of 80–250 nm

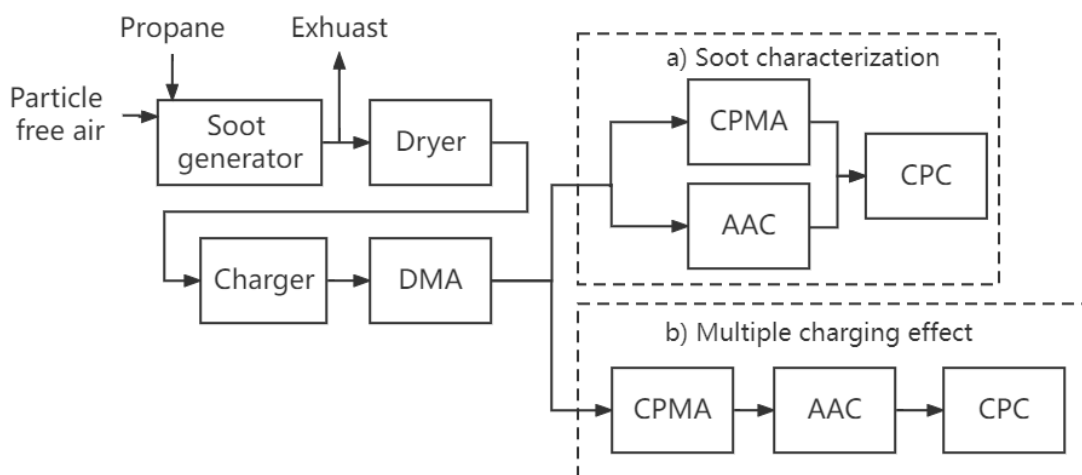
d_m (nm)	m_c (fg)	$d_{ac,c}$ (nm)	$\rho_{DMA-AAC}$ (kg m ⁻³)	$\rho_{DMA-CPMA}$ (kg m ⁻³)	Deviation
80	0.16±0.01	48.2±0.3	551.2±6.9	596.8±37.30	7.65%
100	0.27±0.01	54.8±0.3	488.0±5.32	515.7±19.10	5.38%
150	0.66±0.07	67.8±0.3	359.1±3.22	373.5±39.61	3.86%
200	1.28±0.10	82.1±0.6	303.2±4.44	305.6±23.87	0.77%
250	2.17±0.16	95.9±0.9	262.8±4.92	265.2±19.56	0.90%

577

Table 3. Number concentration fractions and absorption contributions for different size fresh soot particles with single, double or triple charges and the overestimation of MAC accordingly

d_m (nm)	$f_{N,1}$ (%)	$f_{abs,1}$ (%)	$f_{N,2}$ (%)	$f_{abs,2}$ (%)	$f_{N,3}$ (%)	$f_{abs,3}$ (%)	MAC overestimation(%)
80	72.2±2.5	50.6±2.7	26.7±3.0	45.7±4.2	1.1±0.4	3.7±1.5	42.7±9.1
100	82.4±0.5	64.4±0.8	17.6±0.5	35.6±0.8	-	-	28.0±1.8
150	95.8±1.2	87.7±3.1	4.2±1.1	12.3±3.1	-	-	9.2±4.1

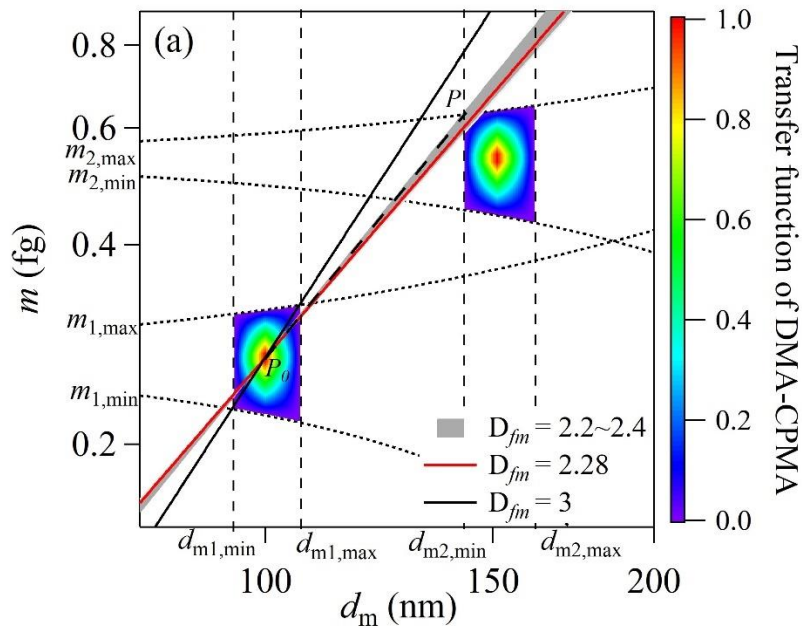
580



581

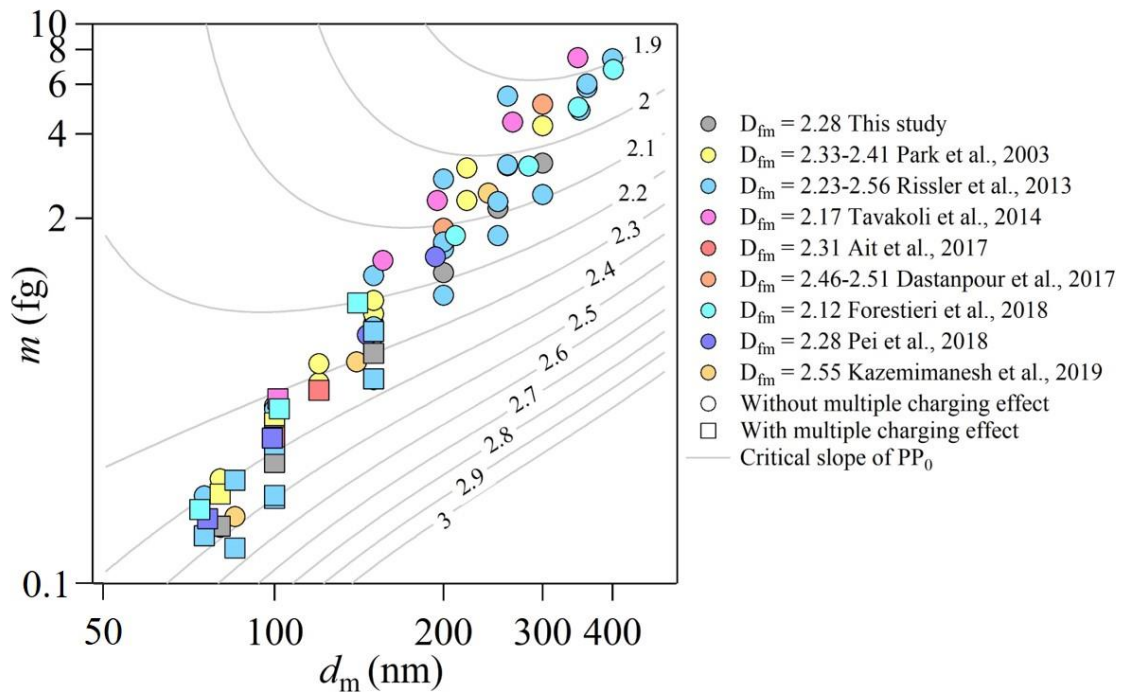
Figure 1: Schematic of the experimental setup: (a) soot characterization and (b) evaluation of multiple charging effects.

583



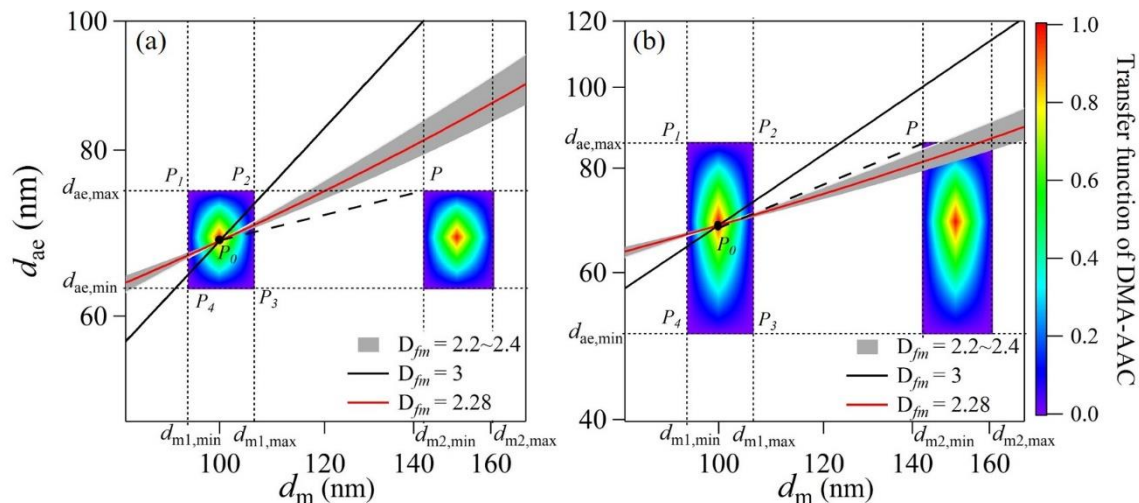
584

585 **Figure 2: Example of the DMA-CPMA transfer function of flame-generated soot particles (Pei et al., 2018) in**
 586 **$\log(m)\text{-}\log(d_m)$. The following parameter set was employed for the calculations: $d_m = 100$ nm, $\beta_{\text{DMA}} = 0.1$, $m = 0.33$**
 587 **fg, $Q_{\text{CPMA}} = 0.3$ L min⁻¹, $R_m = 8$. The color blocks are the transfer function of DMA-CPMA, with the rainbow color**
 588 **representing the transfer function for singly charged (lower left block) and doubly charged (upper right block)**
 589 **particles. The black and red solid lines are particles populations with D_{fm} values of 3 and 2.28, respectively. The**
 590 **gray region is the particle population with D_{fm} of 2.2-2.4, which is typical for soot aerosols. The dotted lines are**
 591 **the limits of d_m and m of DMA and CPMA, respectively. The dashed line is the critical slope of PP_0 . The DMA-**
 592 **CPMA transfer function for +2 particles does not overlap with the line for spherical particles with a single charge**
 593 **($D_{fm}=3$).**



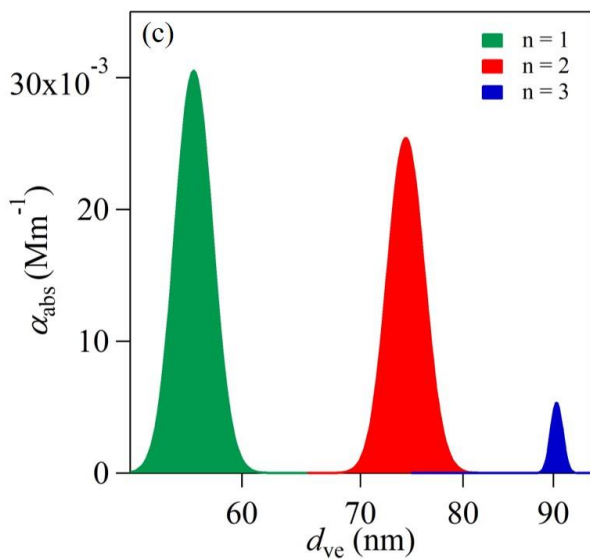
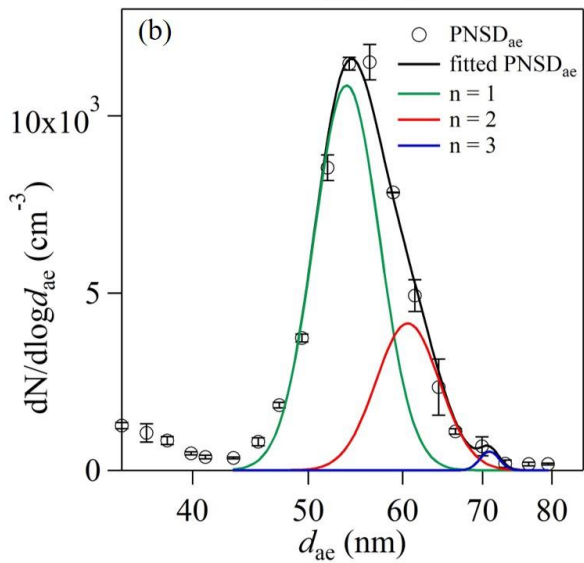
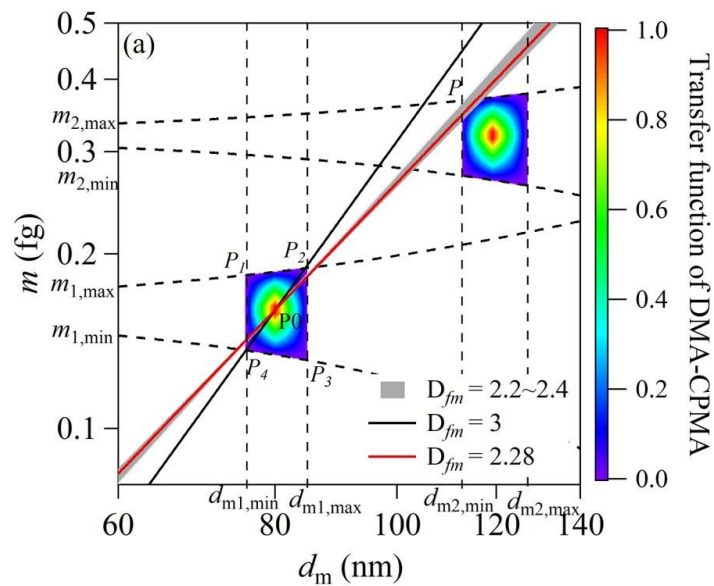
594

595 Figure 3: Variations of the slope of PP_0 as a function of classified d_m and m . The following parameter set was
 596 employed for the calculations: $\beta_{DMA} = 0.1$, $Q_{CPMA} = 0.3 \text{ L min}^{-1}$, $R_m = 8$. The contour lines denote the critical slope
 597 of PP_0 , with values labeled on them. The data points are soot particles measured in the literature (Park et al., 2003;
 598 Rissler et al., 2013; Tavakoli et al., 2014; Ait Ali Yahia et al., 2017; Dastanpour et al., 2017; Forestieri et al., 2018;
 599 Pei et al., 2018; Kazemimanesh et al., 2019) and generated in this study (see details in Sect 3.2). The D_{fm} values of
 600 these data points are listed in the legend. The data points become square when D_{fm} is smaller than the critical
 601 slope of PP_0 in the background, i.e., the potential multiple charging effect may exist.

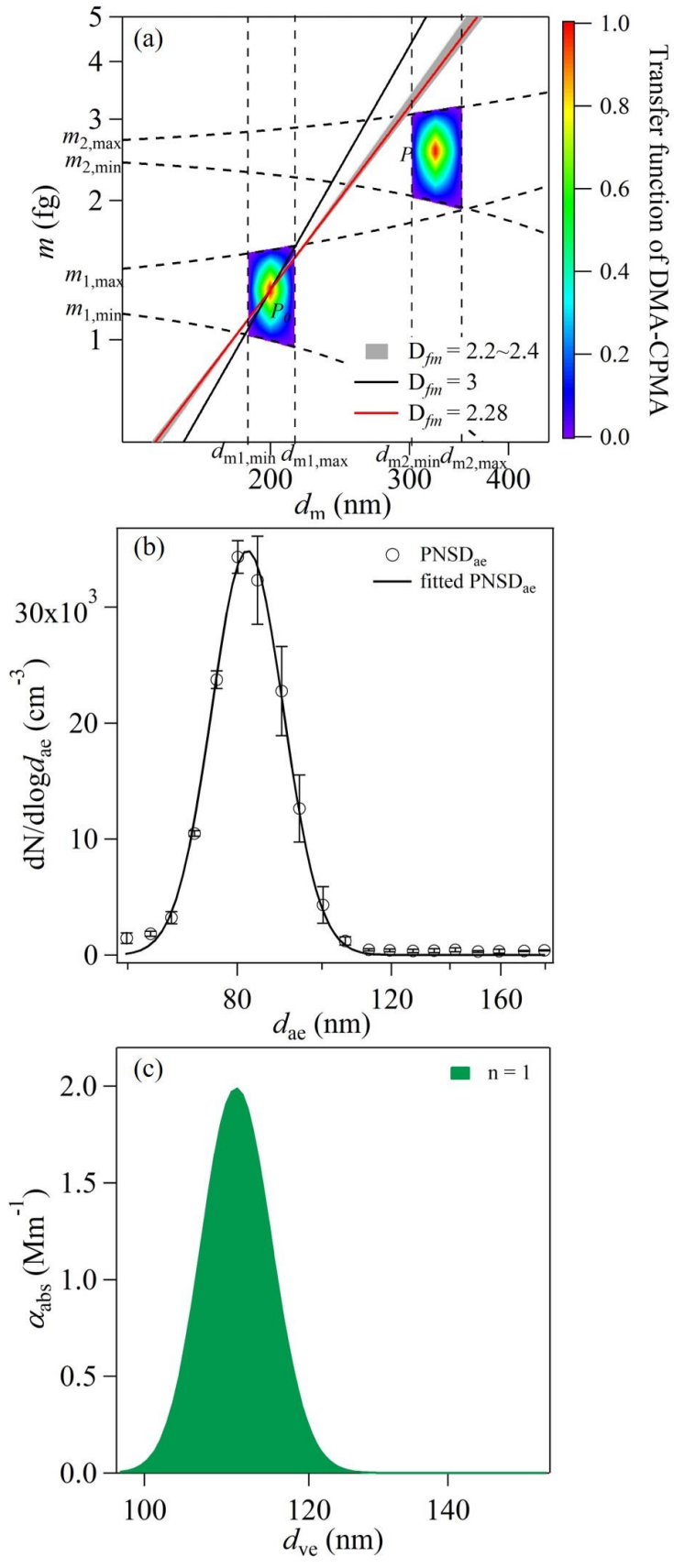


602

603 Figure 4: Examples of transfer function calculation of DMA-AAC of flame-generated soot particles (Pei et al.,
 604 2018). The following parameter set was employed for the calculations: $Q_a = 0.3 \text{ L min}^{-1}$, $d_{m1} = 100 \text{ nm}$, $d_{ae} = 68.3$
 605 nm, (a) $\beta_{DMA} = 0.1$, $\beta_{AAC} = 0.1$, (b) $\beta_{DMA} = 0.1$, $\beta_{AAC} = 0.3$. The color blocks are the transfer functions of DMA-AAC.
 606 The black and red solid lines are particle populations with D_{fm} values of 3 and 2.28, respectively. The gray region
 607 is the particles population with D_{fm} of 2.2-2.4, which is typical for soot aerosol. The dashed line is the critical slope
 608 of PP_0 . The dotted lines are the limiting d_m and d_{ae} of DMA and AAC, respectively.



610 **Figure 5: (a) Transfer functions of DMA-CPMA when selecting 80 nm and 0.16 fg particles. The following**
611 **parameter set was employed for the calculations: $d_{m1} = 80$ nm, $\beta_{DMA} = 0.1$, $m_1 = 0.16$ fg, $Q_{CPMA} = 0.3$ L min⁻¹, $R_m =$**
612 **8. The red solid line is the generated soot particle population. (b) The aerodynamic size distribution of particles**
613 **classified by DMA-CPMA. The circles are data measured by AAC-CPC, and the black, green, red and blue lines**
614 **are log-normal fitted distributions of bulk, singly charged, doubly charged and triply charged particles**
615 **populations. (c) The contributions to light absorption of particles with single, double and triple charges calculated**
616 **with Mie theory.**



618 **Figure 6: (a) The transfer functions of DMA-CPMA when selecting 200 nm and 1.28 fg particles. The following**
619 **parameter set was employed for the calculations: $d_{m1} = 200$ nm, $\beta_{DMA} = 0.1$, $m_1 = 1.28$ fg, $Q_{CPMA} = 0.3$ L min⁻¹, $R_m =$**
620 **8. The red solid line is the generated soot particle population. (b) The aerodynamic size distribution of particles**
621 **classified by DMA-CPMA. The circles are data measured by AAC-CPC, and the solid line is the log-normal fitted**
622 **distribution. (c) Contributions to light absorption of particles with a single charge calculated with Mie theory.**

623